Stability and resistance of nickel catalysts for hydrodeoxygenation

carbon deposition and effects of sulfur, potassium, and chlorine in the feed

Mortensen, Peter Mølgaard; Gardini, Diego; de Carvalho, Hudson W. P.; Damsgaard, Christian Danvad; Grunwaldt, Jan-Dierk; Jensen, Peter Arendt; Wagner, Jakob Birkedal; Jensen, Anker Degn

Published in:
Catalysis Science & Technology

Link to article, DOI:
10.1039/c4cy00522h

Publication date:
2014

Document Version
Publisher's PDF, also known as Version of record

Catalysis Science & Technology

PAPER

View Article Online
View Journal | View Issue

Cite this: *Catal. Sci. Technol.*, 2014, 4, 3672

Stability and resistance of nickel catalysts for hydrodeoxygenation: carbon deposition and effects of sulfur, potassium, and chlorine in the feed†

Peter M. Mortensen,‡[a] Diego Gardini,[b] Hudson W. P. de Carvalho,[c] Christian D. Damsgaard,[bd] Jan-Dierk Grunwaldt,[c] Peter A. Jensen,[a] Jakob B. Wagner[b] and Anker D. Jensen*[a]

Received 22nd April 2014,
Accepted 13th June 2014

DOI: 10.1039/c4cy00522h

www.rsc.org/catalysis

The long term stability and resistance toward carbon deposition, sulfur, chlorine, and potassium of Ni/ZrO_2 as a catalyst for the hydrodeoxygenation (HDO) of guaiacol in 1-octanol (as a model compound system for bio-oil) has been investigated at 250 °C and 100 bar in a trickle bed reactor setup. Without impurities in the feed good stability of the Ni/ZrO_2 catalyst could be achieved over more than 100 h of operation, particularly for a sample prepared with small Ni particles, which minimized carbon deposition. Exposing the catalyst to 0.05 wt% sulfur in the feed resulted in rapid deactivation with complete loss of activity due to the formation of nickel sulfide. Exposing Ni/ZrO_2 to chlorine-containing compounds (at a concentration of 0.05 wt% Cl) on-stream led to a steady decrease in activity over 40 h of exposure. Removal of the chlorine species from the feed led to the regaining of activity. Analysis of the spent catalyst revealed that the adsorption of chlorine on the catalyst was completely reversible, but chlorine had caused sintering of nickel particles. In two experiments, potassium, as either KCl or KNO_3, was impregnated on the catalyst prior to testing. In both cases deactivation was persistent over more than 20 h of testing and severely decreased the deoxygenation activity while the hydrogenation of guaiacol was unaffected. Overall, sulfur was found to be the worst poison, followed by potassium and then chlorine. Thus, removal/limitation of these species from bio-oil is a requirement before long term operation can be achieved with this catalyst.

1. Introduction

Conversion of biomass with flash pyrolysis followed by hydrodeoxygenation has been identified as a prospective path to engine fuels usable in the current infrastructure.[1] In pyrolysis, the biomass is rapidly heated to form char, gas, and a liquid product, the so-called pyrolysis oil or bio-oil. This oil has a low heating value, contains water, is acidic, and has a low shelf storage time, among others, and is therefore not directly suitable as an engine fuel but represents a good energy carrier for bio-energy.[2–4] The unfavorable characteristics of bio-oil are all associated with relatively high oxygen and water content, up to 40 wt% oxygen and 30 wt% water.[1,5]

In hydrodeoxygenation, bio-oil is upgraded with high pressure hydrogen (up to 200 bar) in the presence of a catalyst at temperatures around 300 °C. Hereby the oxygen functionality can be removed, making an oil product more similar to conventional crude oil, which can be used for the production of engine fuels.[1] A challenge in this concept is to find suitable catalysts for HDO which possess good activity and long term stability. Particularly, long term stability is challenging due to the formation of carbon species on the catalysts or due to impurities in the feed.[1,6–10]

Previous work has primarily focused on the traditional hydrotreating catalysts such as $Ni–MoS_2$ and $Co–MoS_2$,[1,11,12] noble metal catalysts based on Pd or Ru,[13–16] or nickel based catalysts[17–21] for HDO. However, little work on these catalytic systems has been devoted to evaluate long term stability or resistance toward impurities during HDO.[1,8,9] Elliott *et al.*[13] tested the stability of HDO of real bio-oil in a continuous flow reactor at 340 °C and 75–130 bar over a Pd/C catalyst and found catalyst lifetimes of up to *ca.* 100 h. They reported carbon build-up and thereby plugging as one of the major problems. Other studies have reported lifetimes of

[a] *Department of Chemical and Biochemical Engineering, Technical University of Denmark, Søltofts Plads, Building 229, DK-2800 Lyngby, Denmark. E-mail: aj@kt.dtu.dk; Fax: +45 4588 2258; Tel: +45 4525 2841*
[b] *Center for Electron Nanoscopy, Technical University of Denmark, Fysikvej, Building 307, DK-2800 Lyngby, Denmark*
[c] *Institute for Chemical Technology and Polymer Chemistry, Karlsruhe Institute of Technology (KIT), Engesserstrasse 20, D-79131 Karlsruhe, Germany*
[d] *CINF, Department of Physics, Technical University of Denmark, Fysikvej, Building 307, DK-2800 Lyngby, Denmark*
† Electronic supplementary information (ESI) available: Reduction temperature, transport evaluation, detailed product composition, and XAFS measurements. See DOI: 10.1039/c4cy00522h
‡ Present address: Haldor Topsøe A/S, Nymøllevej 55, DK-2800 Lyngby, Denmark.

up to 200 h for a Co–MoS_2/Al_2O_3 catalyst.[22] However, from an industrial perspective 100–200 h is a short time.

Carbon on the catalyst is formed because many of the oxy compounds present in bio-oil can undergo polymerization and polycondensation reactions on the catalyst surface, forming polyaromatic species which can lead to the blocking of both the pore structure and the active sites of the catalyst.[23]

As bio-oil is derived from biomass, it will contain traces of a range of inorganic compounds like alkali metals, transition metals, chlorine, sulfur, and phosphorus.[24] Especially, potassium, chlorine, and sulfur can be found in relatively high amounts in bio-oil with concentrations of up to 0.3 wt%, 0.6 wt%, and 0.8 wt%, respectively.[25] These are therefore of significant concern.

In the current work, the long term stability of a Ni/ZrO_2 catalyst has been investigated in a continuous flow setup, using a bio-oil model compound system consisting of guaiacol in 1-octanol. The stability of Ni based catalysts is interesting since much research currently is investigating nickel based catalysts intended for use in HDO of bio-oil[17–20] or lignin and lignosulfonate upgrading.[26,27] It is very well known that nickel based catalysts are particularly prone to sulphur deactivation.[28,29] However, recent results from Song *et al.*[26,27] have, surprisingly, indicated that the high partial pressure of hydrogen used in these reactions might help prevent the deactivation of nickel catalysts due to sulphur. Additionally, Ni/ZrO_2 has been specifically found attractive in a screening study for HDO of phenol.[21] Guaiacol was chosen as the bio-oil model compound to make the interpretation of stability comprehensible, with this molecule representing the phenolic fraction. These are present in significant quantities in bio-oil,[30,31] are among the most persistent molecules of bio-oil,[9,32] and are partly responsible for carbon formation.[9,33] 1-Octanol was chosen as the solvent for guaiacol due to its ideal phase characteristics under the given experimental conditions and furthermore to serve as a simple alcohol model compound.

2. Experimental

2.1 Catalyst synthesis

5 wt% Ni/ZrO_2 was prepared by the incipient wetness method with $Ni(NO_3)_2{\cdot}6H_2O$ (Sigma-Aldrich, ≥97.0%) as the precursor. Zirconia was supplied by Saint-Gobain NorPro and of type SZ 6*152 with an impurity of 3.3% SiO_2, a specific surface area of 140 $m^2\ g^{-1}$, and a pore volume of 0.32 ml g^{-1}. This was initially ground to a particle size of 300–600 μm. In the synthesis, the precursor was dissolved in water equivalent to the pore volume of the support and subsequently mixed with the support. After impregnation, the sample was dried at 70 °C for 12 h. A batch of the catalyst was additionally calcined at 400 °C with a heating rate of 10 °C min^{-1} and a holding time of 4 h.

2.2 Catalytic tests

The experiments were performed in a high pressure gas and liquid continuous flow setup, which is schematically shown in Fig. 1. High pressure liquid is fed from a recirculation loop where a liquid pump and a back pressure valve are used to adjust the feed pressure. From this loop, liquid is fed to the reactor through mass flow controllers and mixed with high pressure gas before reaching the catalyst loaded in the reactor. Liquid samples are withdrawn from a high pressure separator regulated on the basis of the liquid height at 25 °C. The liquid product is collected in a sample manifold placed in a small fume hood, where 8 different samples can be collected as a function of time. Gas from the separator flows through a regulator valve controlling the system pressure, passes a flow meter, and ends at a GC-TCD (GC-2014, Shimadzu). Online sampling on the GC-TCD allows analysis in 20 min intervals.

The reactor tube is made of 316 SS steel and has an inner diameter of 8 mm. This is placed inside a 2 cm inner diameter pressure shell which is placed in a three-zone furnace. The feed gas is introduced in the bottom of the pressure shell and heated in up-flow in the pressure shell before being mixed with the liquid feed in the top flange of the pressure shell and then goes into the reactor tube.

For loading of the reactor tube, 2.5 g of the corresponding catalyst in a sieve fraction of 300–600 μm was mixed with 7.5 g of glass beads in a sieve fraction of 212–245 μm to dilute the catalyst bed and thereby obtain better control of the exothermic reactions. The glass bead–catalyst mixture was suspended on a quartz wool plug in the reactor, which was supported on a crossbar in the reactor. The loading profile of the reactor from the crossbar up was 1 cm of quartz wool, 12 cm of catalyst/glass beads, 1 cm of quartz wool, and 25 cm of glass beads (1 mm in diameter).

All catalysts were initially reduced in the reactor tube by heating at a rate of 10 °C min^{-1} to 500 °C in flow rates of 250 Nml min^{-1} H_2 and 250 Nml min^{-1} N_2 at atmospheric pressure and kept under these conditions for 2 h. 500 °C was sufficient for the complete reduction of Ni/ZrO_2 as found by *in situ* X-ray absorption spectroscopy (XAS) (further information is found in the ESI†). The experimental conditions were set directly after reduction.

Evaluation of transport limitations by Mears criterion[34] for the given sieve fraction of catalyst particles revealed that

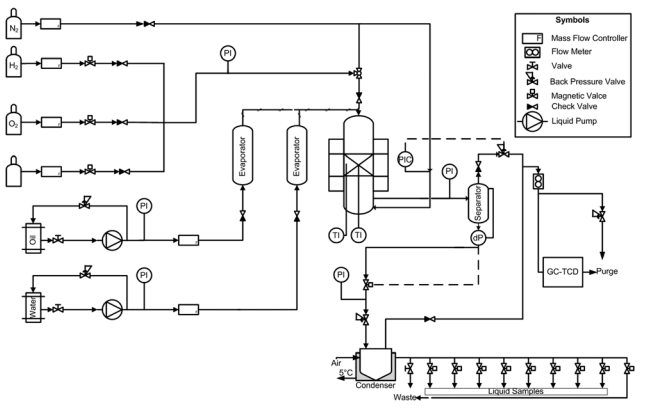

Fig. 1 Flow sheet of the high pressure gas and liquid continuous flow setup used for studying the stability of Ni/ZrO_2 during HDO.

the system was not limited by boundary layer diffusion. However, some internal diffusion resistance was present, at least for the most active catalysts where the effectiveness factor was calculated to be in the range of 0.89–0.97 for the applied particle size distribution. However, as the present work deals with catalyst stability it was concluded that this limitation did not influence the interpretation of the results and may even make the experiments closer to industrial conditions. Additional information on the evaluation of transport limitations can be found in the ESI.†

A feed mixture of 10 vol% guaiacol (Sigma-Aldrich, ≥99%) in 1-octanol (Sigma-Aldrich, ≥99%) was used as the bio-oil model compound system and fed at a flow rate of 0.2 ml min^{-1}. 1-Octanol was chosen as solvent (despite not being considered a bio-oil component) due to its relatively high boiling point (195 °C at ambient pressure[35]) and ability to mix with guaiacol in a homogenous phase. Hydrogen (AGA, 99.9%) and nitrogen (AGA, 99.9%) were fed to the reactor at a flow rate of 300 Nml min^{-1} and 100 Nml ml^{-1}, respectively, corresponding to 6 times the required hydrogen for complete hydrogenation and deoxygenation of the feed. During the reactions the reactor was maintained at a constant pressure of 100 bar and the set point of the reactor oven was 250 °C for all experiments. The actual temperature in the catalyst bed varied between 245 °C in the bottom of the bed and 251 °C in the top part. The slightly higher temperature in the top part of the bed was due to the exothermic reactions taking place.

In the deactivation experiments either 1-octanethiol (Sigma-Aldrich, ≥98.5%) or 1-chlorooctane (Sigma-Aldrich, 99%) was added to the liquid feed corresponding to a concentration of 0.05 wt% S or Cl, respectively. Assuming 100% decomposition to H_2S or HCl, this would correspond to concentrations of 177 ppm_v and 162 ppm_v in the feed gas, respectively.

KCl or KNO_3 was impregnated to separate batches of the catalyst by incipient wetness impregnation. A portion of the uncalcined Ni/ZrO_2 catalyst was weighed and a solution (corresponding to the pore volume of the given fraction of the catalyst) with KCl or KNO_3 in H_2O was prepared. KCl and KNO_3 were impregnated in amounts corresponding to the molar content of nickel. After mixing the solution and the catalyst, it was dried for 12 h at 70 °C.

A blank experiment without the catalyst was performed under the same conditions as the experiments. This led to a conversion of 2% for guaiacol and hardly any conversion of 1-octanol, showing that the reactor was not catalytically active for the reaction.

2.3 Product analysis

Analysis of the liquid product was done with a Shimadzu GC-MS/FID-QP2010 Ultra EI gas chromatograph fitted with a Supelco Equity-5 column. Identification of the products was done using a mass spectrometer (MS) where their concentration was quantified using a flame ionization detector (FID). External standards were prepared for guaiacol, cyclohexanol, cyclohexane, methanol, 1-octanol, and heptane. The concentrations of the remaining peaks were calculated from the FID on the basis of the effective carbon number method,[36] where the concentration of a compound was found as:

$$C_i = C_{ref} \cdot \frac{A_i}{A_{ref}} \frac{\nu_{eff,ref}}{\nu_{eff,i}} \quad (1)$$

Here C is the concentration, A the area of the peak in the FID spectrum, and ν_{eff} the effective carbon number. Index i refers to the compound with the unknown concentration and index ref refers to a reference compound where the concentration is known. In all calculations with this formula, heptane was used as reference. The effective carbon number was taken from the review by Schofield.[36]

The conversion, X, was calculated as:

$$X = \left(1 - \frac{C_{out,i} \cdot \nu_{out}}{C_{0,i} \cdot \nu_0}\right) \cdot 100\% \quad (2)$$

Here C_i is the concentration of compound i and ν is the volumetric flow. Index out refers to the conditions after the reactor, index 0 refers to the inlet conditions, and i refers to the compound of relevance. The conversions of both guaiacol and 1-octanol were evaluated.

The yields (Y_i) of relevant products were calculated as:

$$Y_i = \frac{C_{out,i} \cdot \nu_{out}}{C_{0,j} \cdot \nu_0} \cdot 100\% \quad (3)$$

Index i here refers to the compound of relevance and index j refers to the initial reactant, guaiacol or 1-octanol.

The selectivity (S_i) of a compound (i) was calculated as:

$$S_i = \frac{Y_i}{X} \cdot 100\% \quad (4)$$

The degree of deoxygenation (DOD) was calculated as:

$$DOD = \left(1 - \frac{F_{O,out}}{F_{O,in}}\right) \cdot 100\% \quad (5)$$

Here F_O is the molar flow of oxygen in oxygen-containing species except water either in or out of the reactor. To give further emphasis on the HDO of guaiacol, which only constituted 10% of the feed, the degree of deoxygenation for the guaiacol related compounds (DOD^{GUA}) was also calculated:

$$DOD^{GUA} = \left(1 - \frac{\sum_i F_{O\ of\ i,out}}{2 \cdot F_{Guaiacol,in}}\right) \cdot 100\% \quad (6)$$

Here index i refers to the oxygen-containing guaiacol related compounds, which were guaiacol, methanol, cyclohexanol, and 2-methoxy-cyclohexanol.

The carbon balance was evaluated on the basis of the GC-MS/FID and GC-TCD measurements:

$$\Delta C = \left(\frac{\sum_i \nu_i \cdot F_i - 7 \cdot F_{0,\text{Guaiacol}} - 8 \cdot F_{0,\text{1-Octanol}}}{7 \cdot F_{0,\text{Guaiacol}} + 8 \cdot F_{\mathbf{0},\text{1-Octanol}}} \right) \cdot 100\% \qquad (7)$$

Here ΔC is the carbon deviation in % and F_i is the molar flow of compound i. All compounds identified in the GC-MS/FID and GC-TCD analyses were included in the carbon balance. Generally the carbon balance was closed within 5%. This will be discussed in further detail later.

2.4 Catalyst characterization

The specific surface area was estimated by a seven-point BET measurement (Quantachrome iQ2).[37] Nitrogen adsorption at its boiling point was used in the p/p_0 range of 0.05–0.3. The produced Ni/ZrO_2 catalyst had a specific surface area of 130 $m^2\ g^{-1}$.

The local structure of the catalysts was characterized by XAS in terms of X-ray absorption near edge structure (XANES) and extended X-ray absorption fine structure (EXAFS) at the Ni-K edge at the XAS beamline at the synchrotron radiation source ANKA (Karlsruhe, Germany). The reduction of Ni/ZrO_2 was followed *in situ*, whereas the structures of the poisoned catalysts were analyzed *ex situ* after the corresponding reactions.

The catalyst reduction was followed by Quick-XAS in fluorescence detection mode.[38] For this purpose, a 63–125 μm sieved fraction of the calcined catalyst was filled into a quartz capillary microreactor (1 mm internal diameter) resulting in plug flow-like conditions.[39] The reaction mixture, 25% H_2 in He, in a flow rate of 50 mL min^{-1} was supplied by a gas delivery system. The microreactor was heated with a gas blower (FMB Oxford) from room temperature up to 500 °C using a heating rate of 5 °C min^{-1} similar to the setup in ref. 40. Spectra were recorded every 12.5 °C.

The *ex situ* studied catalysts were pressed to pellets using cellulose and then measured in transmission mode.

XAS data analysis was carried out using Athena and Artemis softwares of IFEFFIT.[41] The spectra were energy calibrated from a reference metal foil and the background was subtracted and then normalized. The structural parameters were obtained by adjusting theoretical backscattering phases and amplitudes (*ab initio* calculated with FEFFG).[42]

The relative proportions between the starting and the formed Ni species were estimated by linear combinations carried out using Athena IFEFFIT software.[41] Linear combination fitting was performed in the spectral range of −20 to 90 eV relative to the energy of the edge. This procedure allowed tracking the proportion of species consumed and formed during catalyst activation. The references for the linear combinations were the first spectrum at room temperature and the last spectrum at 500 °C.

Powder X-ray diffraction (XRD) measurements were carried out using a PANalytical X'Pert PRO diffractometer in a Bragg–Brentano Theta–Theta geometry. A 300–600 μm sieved fraction of the catalyst was analyzed at a $25° < 2\theta < 100°$ range using monochromatic Cu-Kα radiation (λ = 1.5418 Å). XRD data treatment was carried out using PANalytical HighScore Plus 3.0.5 and the average crystallite size was estimated using the Scherrer equation. The crystallite size analysis was carried out neglecting the lattice strain effects.

The elemental composition of the catalysts was analyzed by means of energy dispersive X-ray spectroscopy (EDX) with an FEI Quanta 200 ESEM FEG scanning electron microscope (SEM) operated at 10 kV and equipped with an Oxford Instruments 80 mm^2 X-Max silicon drift detector. A few particles of 300–600 μm sieved fractions of the catalyst were fixed to standard SEM aluminium stubs with Vishay Micro-Measurements M-Bond epoxy resin and mechanically polished in order to reach a flat geometry configuration.

EDX elemental maps were acquired using a FEI Osiris transmission electron microscope (TEM) operated at 200 kV in scanning mode (STEM). Catalysts were crushed in a mortar and dry dispersed on a copper TEM grid coated with lacey carbon. Maps were smoothed using a 7 × 7 pixels kernel smoothing algorithm implemented in the Bruker Esprit software.

Temperature programmed oxidation (TPO) was performed in a tubular furnace. Prior to the analysis the spent catalyst samples were washed in ethanol and dried. 50–100 mg of the catalyst was placed in a ceramic boat and placed in the center of the oven and heated at a ramp of 11 °C min^{-1} in a flow rate of 1100 Nml min^{-1} gas (10% oxygen in nitrogen). Online CO and CO_2 measurements were performed with an IR detector (ABB automation GmbH AO2020 Uras26) in order to quantify the amount of carbon on the catalyst. Carbon determination was done on the basis of the integration of the CO/CO_2 signal relative to flow and time.

Elemental analysis of nickel on the catalysts was performed using inductively coupled plasma atomic emission spectroscopy (ICP-OES). For the analysis, the samples were crushed and melted together with potassium pyrosulfate. This was dissolved in a solution of water and HCl and then analyzed by plasma emission spectroscopy. The instrument was calibrated with a certified nickel standard.

3. Kinetic model

For a more quantitative description of the catalyst activity a kinetic model was developed for the HDO of guaiacol and 1-octanol.

On the basis of the product distributions (see ESI†), guaiacol was indicated to react by the sequential reaction scheme shown in Fig. 2. Guaiacol was initially hydrogenated to 2-methoxy-cyclohexanol, followed by hydrogenolysis of the ether bond to form cyclohexanol and methanol. Both alcohols can subsequently undergo hydrodeoxygenation to produce, respectively, cyclohexane and methane. The same reaction scheme has been observed for the HDO of guaiacol over noble metal catalysts,[43–45] indicating that this is a general reaction path over transition metal catalysts.

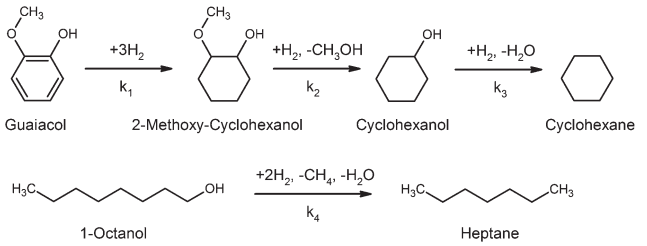

Fig. 2 Observed reaction path of guaiacol and 1-octanol.

Heptane was the primary product from 1-octanol (as shown in Fig. 2), and therefore a cracking type reaction appeared to be the primary path for this compound. Previous work on Pt catalysts with C_3 alcohols[46,47] has shown that these undergo an initial dehydrogenation to form an aldehyde, which can then undergo decarbonylation producing ethane and CO. Probably, the same reaction pathway occurs for 1-octanol over nickel catalysts. However, under the conditions used in our experiments, the CO produced can be hydrogenated into CH_4. Note that the Gibbs free energy of the reaction $CO + 3H_2 \leftrightarrow H_2O + CH_4$ is -96.4 kJ mol^{-1} at 500 K (calculated with the data from ref. 48), and the equilibrium is completely displaced toward CH_4 formation. This could explain why only CH_4 was detected in the gas phase.

Based on the experimental observations summarized in Fig. 2, the reaction rates of the four identified main reactions were assumed to be:

$$r_1 = k_1 \cdot C_{\text{Guaiacol}} \cdot P_{H_2}{}^{n} \quad (8)$$

$$r_2 = k_2 \cdot C_{\text{2-Methoxy-cyclohexanol}} \cdot P_{H_2}{}^{m} \quad (9)$$

$$r_3 = k_3 \cdot C_{\text{Cyclohexanol}} \cdot P_{H_2}{}^{l} \quad (10)$$

$$r_4 = k_4 \cdot C_{\text{1-Octanol}} \cdot P_{H_2}{}^{k} \quad (11)$$

Here r_i is the rate of reaction i, k_i is the rate constant for reaction i, C_i is the concentration of compound i in the liquid phase, P_{H_2} is the partial pressure of H_2, and n–k are the unknown reaction orders of hydrogen. All hydrocarbon reaction orders were assumed 1st order. Previous work has shown that 1st order reactions of guaiacol, anisole, and phenol HDO sufficiently describe these systems for simple interpretations.[19,21,49]

As a significant excess of hydrogen was used in all experiments the partial pressure of hydrogen was assumed constant and therefore the kinetic expressions were reduced to:

$$r_1 = k_1' \cdot C_{\text{Guaiacol}} \quad (12)$$

$$r_2 = k_2' \cdot C_{\text{2-Methoxy-cyclohexanol}} \quad (13)$$

$$r_3 = k_3' \cdot C_{\text{Cyclohexanol}} \quad (14)$$

$$r_4 = k_4' \cdot C_{\text{1-Octanol}} \quad (15)$$

Based on these rate terms a kinetic model was derived for a plug flow reactor system. The derivation of this model can be found in the ESI.†

4. Results and discussion

4.1 Long term stability

Two batches of 5 wt% Ni/ZrO_2 were prepared: one where the batch was calcined at 400 °C for 4 h and one where the batch was not calcined. Both samples were reduced at 500 °C as found from the analysis in the ESI.† In this way two different nickel particle sizes could be obtained, as described by Louis *et al.*[50] In the following, Ni/ZrO_2-CR will refer to the calcined and reduced sample and Ni/ZrO_2-DR will refer to the directly reduced sample.

Representative STEM-EDX elemental maps for both Ni/ZrO_2-CR and Ni/ZrO_2-DR are shown in Fig. 3(a) and (b), respectively. From these and other acquired maps it was possible to estimate the Ni particle size being on average 9 nm for Ni/ZrO_2-DR and 18 nm for Ni/ZrO_2-CR based on size measurements of more than 80 particles for each catalyst (size distributions are shown in Fig. 4). Although the number of analyzed particles cannot be considered fully statistically representative, the size distribution for Ni/ZrO_2-DR was noticed to be more homogenous than that for Ni/ZrO_2-CR. For the calcined sample, a tail toward larger particle sizes and the presence of very big ones (>100 nm) were observed (*cf.* Fig. 4(a)), indicating agglomeration of some nickel during the preparation procedure. It is worth mentioning that using the Ni signal to estimate the average particle size does not take into account any oxidation effect that could occur by exposure of the sample to air. However, XRD measurements did not reveal any evident oxidation of the Ni nanoparticles.

The two catalysts were tested at 250 °C and 100 bar with a feed of 0.2 ml min^{-1} and 10 vol% guaiacol in 1-octanol corresponding to a WHSV of 4.0 h^{-1}. In Fig. 5(a) and (b) the development in the conversion of guaiacol and 1-octanol and the degree of deoxygenation (DOD) is shown as a function of time on stream (TOS) for both catalysts.

For Ni/ZrO_2-CR (*cf.* Fig. 5(a)) a maximum DOD of 40% was achieved after 3.5 h of TOS and hereafter the activity decreased throughout the 80 h of TOS, ending at 23% DOD. The relative decrease of DOD^{GUA} was more pronounced, from a value of 17% to only 4% after 80 h TOS. Thus, little deoxygenation of the guaiacol was found at the end of the experiment.

For Ni/ZrO_2-DR (*cf.* Fig. 5(b)) the DOD was significantly higher, in the order of 90%. Also the stability of this catalyst was better, as the DOD^{GUA} only decreased from a value of 71% to 61% after 104 h TOS.

Both catalysts converted all guaiacol into 2-methoxy-cyclohexanol as a first step. However, the selectivities toward subsequently formed cyclohexanol and cyclohexane were only *ca.* 30% and *ca.* 1% on Ni/ZrO_2-CR, respectively, but *ca.* 50% and *ca.* 25% on Ni/ZrO_2-DR, respectively (detailed development in the yield of 2-methoxy-cyclohexanol, cyclohexanol,

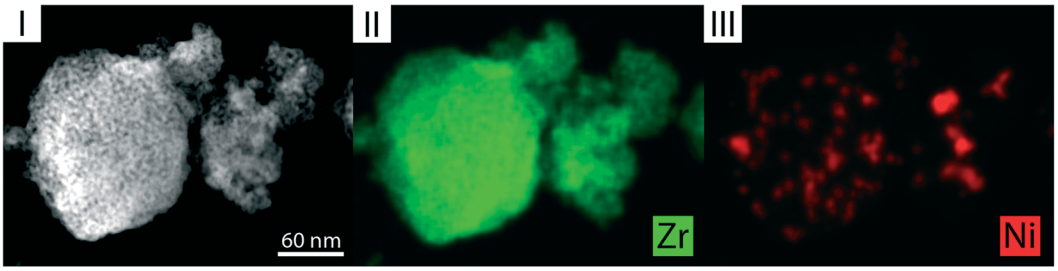

(a) STEM-HAADF micrograph of Ni/ZrO_2-CR

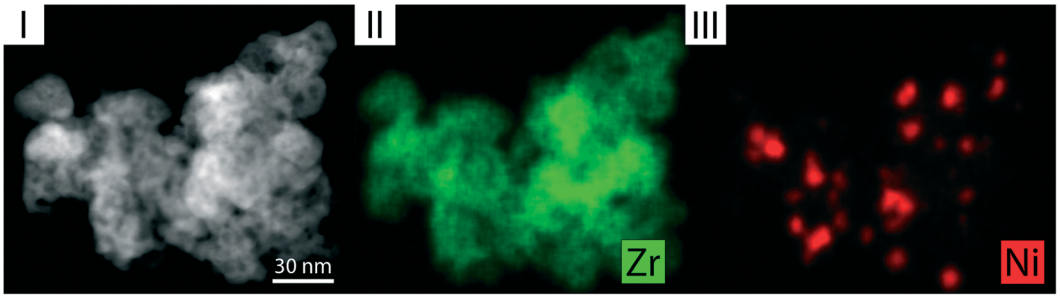

(b) STEM-HAADF micrograph of Ni/ZrO_2-DR

Fig. 3 STEM-HAADF micrographs of Ni/ZrO_2-CR (a) and Ni/ZrO_2-DR (b). Sub-image I: STEM-HAADF micrograph. Sub-image II: zirconium EDX elemental distributions. Sub-image III: nickel EDX elemental distributions.

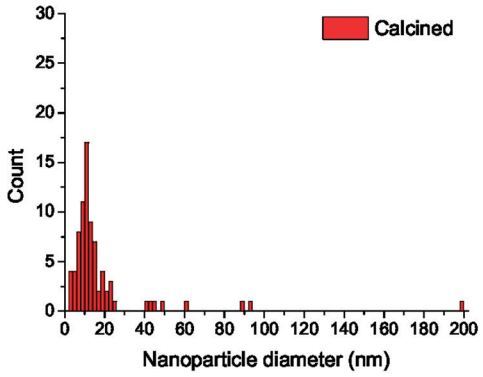

(a) Ni/ZrO_2-CR size distribution

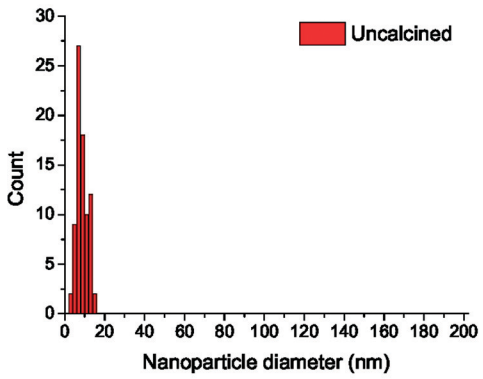

(b) Ni/ZrO_2-DR size distribution

Fig. 4 Size distributions of Ni/ZrO_2-CR (a) and Ni/ZrO_2-DR (b) based on the STEM-HAADF images.

cyclohexane, and heptane can be found in the ESI†). Similarly, the conversion of 1-octanol was around 30% on Ni/ZrO_2-CR but 100% on Ni/ZrO_2-DR. In both cases >90% selectivity toward heptane was observed.

Using the simple kinetic model in section 3, the catalytic activity of the catalysts was quantified, as summarized in Table 1. The rate of hydrogenation (k_1') could not be distinguished on the two catalysts, as both had 100% conversion. However, the rate of the three deoxygenation reactions (k_2', k_3', and k_4') were a factor of 2.4, 6.9, and approximately 10 times higher for Ni/ZrO_2-DR compared to Ni/ZrO_2-CR, respectively.

The large difference in activity can be linked to the difference in nickel particle size on the catalysts. In our previous study,[51] we have shown that the deoxygenation activity of nickel based catalysts can be increased by decreasing the nickel crystallite size due to an increasing fraction of step/corner sites on the nickel nanoparticles, which are more active for the C–O bond breaking reaction. Thus, Ni/ZrO_2-DR would also be expected to have the highest activity. Comparing the individual rate constants, the decarbonylation reaction and the deoxygenation reaction were most dependent on the type of nickel sites available, as k_3' and k_4' had the largest relative increase. In contrast, the hydrogenolysis reaction (k_2') was less structure sensitive, which may be linked to a lower bond dissociation energy of the methoxy group (343 kJ mol^{-1} (ref. 52)) compared to that of the alcohol group (385 kJ mol^{-1} (ref. 52)).

Detailed analysis of the GC-MS/FID data revealed that the side products included methanol, cyclopentane, cyclopentanol, octane, methoxy-cyclohexane, cyclohexanone, dicyclohexyl ether, and dioctyl ether. A complete carbon analysis from the experiment with Ni/ZrO_2-DR (*cf.* Fig. 5(b)) showed that 91% of the carbon fed to the reactor was recovered in the oil phase,

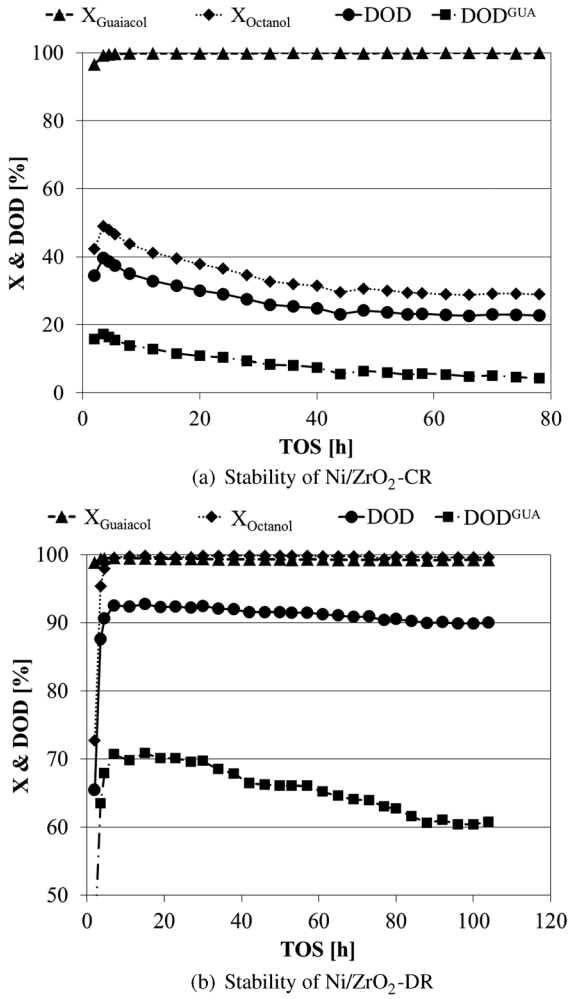

Fig. 5 Development of the conversions of guaiacol and 1-octanol and DOD for Ni/ZrO_2-CR (a) and Ni/ZrO_2-DR (b) as a function of TOS. DOD^{GUA} is the degree of deoxygenation of the guaiacol feed. Ni/ZrO_2-CR was calcined and then reduced while Ni/ZrO_2-DR was not calcined but reduced directly from nickel nitrate. T = 250 °C, P = 100 bar, F_{oil} = 0.2 ml min^{-1}, WHSV = 4.0 h^{-1}.

Table 1 Comparison between Ni/ZrO_2-CR and Ni/ZrO_2-DR, summarizing kinetic parameters, nickel particle size, and carbon build-up on the spent catalysts. Ni/ZrO_2-CR was calcined and then reduced while Ni/ZrO_2-DR was not calcined but reduced directly from nickel nitrate. Kinetic parameters evaluated at TOS = 4.5 h for Ni/ZrO_2-CR and TOS = 10 h for Ni/ZrO_2-DR. Carbon content measured on the basis of temperature programmed oxidation (TPO)

Catalyst	Ni/ZrO_2-CR	Ni/ZrO_2-DR
Total TOS [h]	79	106
Crystallite size [nm]	18	9
Carbon content [wt%]	3.7	1.5
Carbon content [mol C mol^{-1} Ni]	3.6	1.5
Carbon deposition rate [$\mu g_C\ g_{cat}^{-1}\ h^{-1}$]	463	144
k_1' [ml $kg_{cat}^{-1}\ min^{-1}$]	≥500	≥500
k_2' [ml $kg_{cat}^{-1}\ min^{-1}$]	51	126
k_3' [ml $kg_{cat}^{-1}\ min^{-1}$]	11	76
k_4' [ml $kg_{cat}^{-1}\ min^{-1}$]	52	≥500

1% in the aqueous phase, and 6% in the gas phase; the remaining 2% was unaccounted for. The aqueous phase contained methanol, cyclohexanol, and 2-methoxy-cyclohexanol as primary carbon-containing species. Loss of carbon to the gas phase was due to the formation of CH_4, which was linked to the reduction of methanol formed from guaiacol and the hydrogenation of CO from 1-octanol (see discussion in section 3).

In order to quantify the carbon on the spent catalyst, the used catalysts were subjected to TPO (*cf.* results in Table 1). For both catalysts the deposited carbon was oxidized in the temperature range of 200–500 °C with a peak in the CO/CO_2 evolution just below 400 °C. Comparing Ni/ZrO_2-DR to Ni/ZrO_2-CR, Ni/ZrO_2-CR had 3 times higher carbon deposition rate. This correlates with a more pronounced deactivation on Ni/ZrO_2-CR as a function of TOS (*cf.* Fig. 5(a)).

Borowiecki[53] showed that the carbon deposition rate during steam reforming of butane at 500 °C was highly dependent on the nickel crystallite size, increasing by more than an order of magnitude when increasing the nickel crystallite size from 6.5 nm to 35.7 nm. Bengaard *et al.*[54] later described that carbon nucleation takes place on the step sites on the nickel crystals and builds carbon layers from there. These layers are however only thermodynamically stable when the carbon layer is larger than ≈25 Å and therefore the associated nickel facet, on which the carbon layer is built, should be larger than this. Increasing the carbon layer size further decreases the total energy and therefore stabilizes carbon formation further. Thus, large nickel particles are in other contexts also found more prone to carbon formation.[53–55]

Another potential source of deactivation is the loss of active metal by leaching. Therefore, the nickel content was investigated in one case for Ni/ZrO_2-DR by ICP-OES. Prior to reduction, this catalyst had a nickel content of 4.5–4.9 wt%; the span is indicated because Ni/ZrO_2-DR contained some fraction of NO_3 which should be corrected for in the comparison. After 104 h of operation the nickel content was again measured to be 4.7 wt%. Hence, the extent of nickel leaching from the catalyst is negligible.

In conclusion, carbon deposition appears to be the most probable cause for the observed loss of activity in Fig. 5. This is supported by the observation that the rate of deactivation is faster on Ni/ZrO_2-CR compared to Ni/ZrO_2-DR, which correlates with the threefold higher carbon build-up rate on Ni/ZrO_2-CR compared to Ni/ZrO_2-DR.

4.2 Effect of impurities in the feed

To understand other potential deactivation mechanisms during the HDO of bio-oil, exposure to sulfur, chlorine, and potassium in the feed was simulated, as described in the following. Ni/ZrO_2-DR was used for all of these measurements due to the higher activity of this sample.

4.2.1 Effect of sulfur. In an experiment similar to those discussed in section 4.1, 0.3 vol% 1-octanethiol (corresponding to 0.05 wt% S in the feed) was added to the feed with 10% guaiacol in 1-octanol after 8 h of TOS. This impurity of sulfur is representative of what can be present in bio-oil.[25] Fig. 6(a)

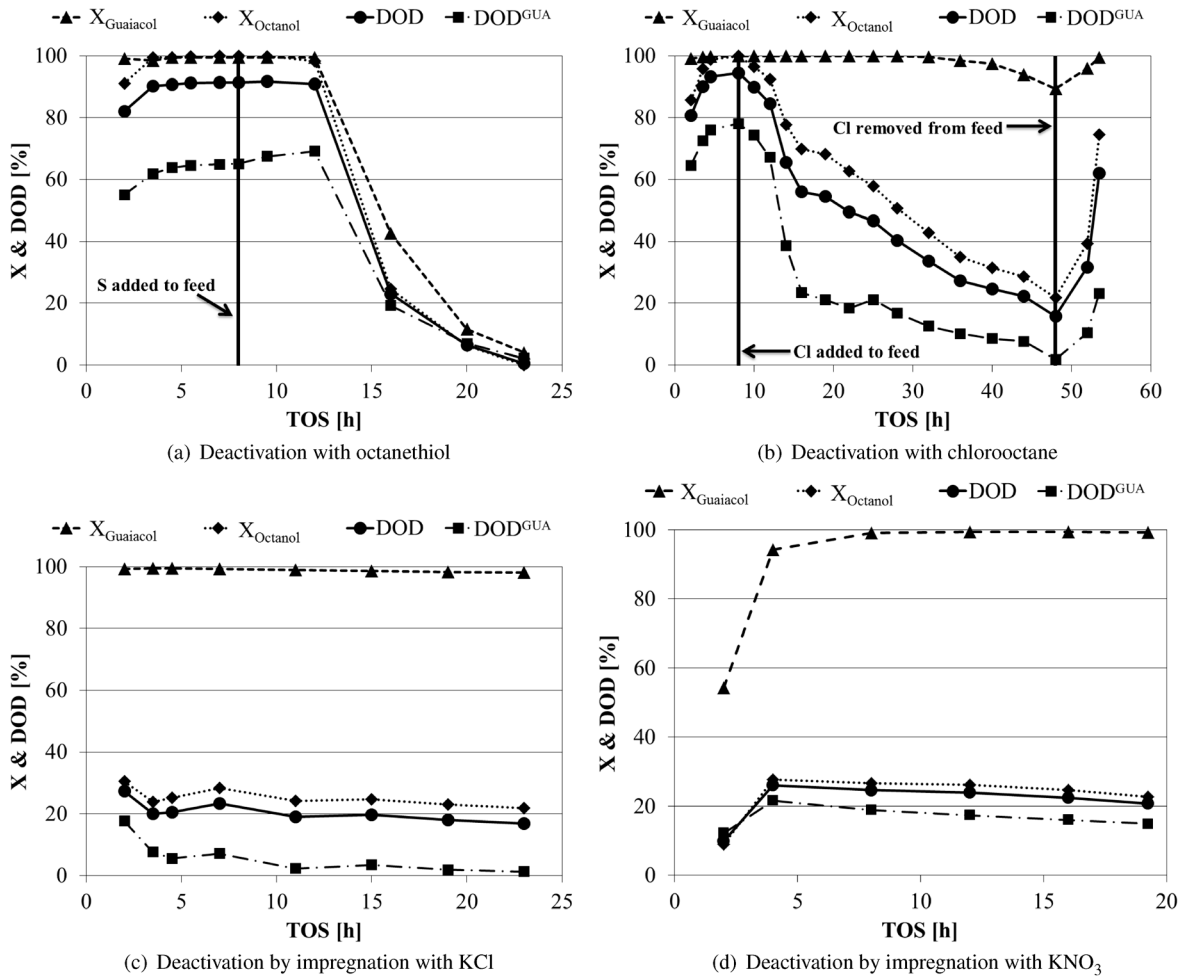

Fig. 6 Development of the conversions of guaiacol and 1-octanol and DOD over the Ni/ZrO_2-DR catalyst as a function of time when deactivated with 1-octanethiol (a), 1-chlorooctane (b), KCl (c), and KNO_3 (d). 1-Octanethiol and 1-chlorooctane were added to the feed in concentrations of 0.05 wt% S and 0.05 wt% Cl, respectively, after 8 h of TOS as indicated in the respective figures. 1-Chlorooctane was removed from the feed again after 48 h of TOS, as shown in Fig. 6(b). KCl or KNO_3 were impregnated in stoichiometric amounts relative to nickel on a fresh batch of catalyst prior to testing. DOD^{GUA} is the degree of deoxygenation isolated for the guaiacol feed. T = 250 °C, P = 100 bar, F_{oil} = 0.2 ml min^{-1}, WHSV = 4.0 h^{-1}.

shows the development in the conversion of guaiacol and 1-octanol and the DOD as a function of TOS. Initially, when sulfur was not present, the conversions of both 1-octanol and guaiacol were 100% and the DOD was in the order of 90–92%, similar to the experiment with no impurities present (*cf.* Fig. 5(b)). After the introduction of sulfur, the activity rapidly decreased. After only 12 h exposure to sulfur the conversions of both guaiacol and 1-octanol were almost 0%. The conversion of both compounds and the DOD decreased in a similar way, indicating that deactivation was taking place as a progressive front in the catalyst bed, inhibiting all types of reactions as the sulfur front progressed. The relative exposure to sulfur over the entire experiment was 1.1 mol S : mol Ni, showing an effective deactivation by sulfur.

1-Octanethiol was quantitatively converted to heptane or octane and H_2S throughout the experiment. Only in the final two liquid samples, where the activity had severely decreased, traces of 1-octanethiol could be found.

4.2.2 Effect of chlorine. In a similar experiment to the one described above, a new batch of catalyst was loaded and started with a standard feed of 10 vol% guaiacol in 1-octanol. After 8 hours of operation the feed was changed to 10 vol% guaiacol and 0.3 vol% 1-chlorooctane (corresponding to 0.05 wt% Cl in the feed) in 1-octanol. This corresponds to the quantity of organic bound chlorine, which can be found in bio-oil.[25] In Fig. 6(a) the development in the conversion of guaiacol and 1-octanol and the DOD is seen as a function of TOS. Initially, the activity was similar to the reference case (*cf.* Fig. 1) with no impurities in the feed, but after the introduction of chlorine to the feed the activity of deoxygenation steadily decreased; the DOD decreased from a level of 90–95% to 16% after 40 h exposure to the chlorine-containing feed. However, the DOD^{GUA} decreased even faster and dropped to below 25% after only 8 h of exposure.

The conversion of 1-octanol followed the development in the DOD. In contrast, the conversion of guaiacol was only

slightly affected, dropping a few percentage points only after 30 h of exposure. With respect to the product composition, the yield of cyclohexane decreased from 40% prior to deactivation to only a few percent after *ca.* 10 h exposure to chlorine. The cyclohexanol yield was not affected to the same extent and only decreased from a yield of 32% to 17% after 40 h of exposure. 2-Methoxy-cyclohexanol ended up being the primary product with a yield of more than 70% (see ESI†). Thus, chlorine deactivation is primarily associated with the deoxygenation activity of the catalyst.

Throughout the chlorine exposure period there was a complete conversion of 1-chlorooctane to heptane and HCl. Nickel has also previously been reported as effective in the hydrodechlorination (HDCl) reaction.[56–59] The exposure to chlorine atoms has therefore been high throughout the exposure period.

After 48 h of TOS the feed was changed back to the chlorine-free feed (10 vol% guaiacol in 1-octanol). At this point the activity increased (*cf.* Fig. 6(b)) toward the initial activity level before terminating the experiment. Thus, the deactivation by chlorine appears to be at least partly reversible, indicating that the Cl species blocking the surface sites required for HDO can desorb. The desorption of chlorine from the catalyst was further proven by verification of Cl^- in the liquid product collected at a TOS of 51–52 h by precipitation with $AgNO_3$.

In the 40 h where chlorine was fed to the reactor the relative exposure was 3.2 mol Cl : 1 mol Ni. All of this shows that the deactivation by chlorine was not as persistent as that by sulfur, which is probably linked to reversible adsorption.

4.2.3 Effect of potassium. In the third type of deactivation experiment, KCl was impregnated on a batch of Ni/ZrO_2-DR in stoichiometric amounts relative to nickel on the catalyst. Fig. 6(c) shows the conversions of guaiacol and 1-octanol and the DOD as a function of TOS for this catalyst. In this experiment the DOD was in the order of 20%, the conversion of guaiacol was 100% throughout 24 h of TOS, while the conversion of 1-octanol was in the order of 25%. The primary part of deoxygenation was from 1-octanol, as the DOD^{GUA} was only around 5% with the 2-methoxy-cyclohexanol yield being 76% (see ESI†). Thus, similar to the Cl deactivated catalyst, KCl deactivated mainly the deoxygenation reactions. However, in contrast to the Cl deactivated case this catalyst was persistently deactivated as the DOD was constantly low throughout the 24 h experiment.

The isolated effect of potassium was tested by impregnation of a batch of Ni/ZrO_2-DR with stoichiometric amounts of KNO_3 relative to nickel. In Fig. 6(d) the conversions of guaiacol and 1-octanol and the DOD are shown as a function of TOS in a 20 h experiment. Comparing to Fig. 6(c) with KCl deactivation, similar trends are seen: the conversion of guaiacol was high (100%) throughout the test, 2-methoxy-cyclohexanol was the primary product (56% selectivity) from guaiacol, and deactivation was persistent as the activity was stable throughout 20 h of TOS. However, the DOD^{GUA} was around 10–15% for the KNO_3 deactivated sample compared to 5% in the KCl case, and therefore the interaction with the guaiacol molecule was more hampered in the latter case.

4.3 XRD and TEM characterization of poisoned catalysts

4.3.1 Sulfur poisoning. The presence of sulfur in the spent catalyst was confirmed by STEM-EDX elemental maps, showing a very similar spatial distribution of sulfur and nickel signals (*cf.* Fig. 7). Thus, it appears that sulfur preferentially adsorbed on the nickel.

XRD measurements (*cf.* Fig. 8(a)) revealed the presence of zirconia and a reflection at $2\theta \approx 45.2°$ could be identified as NiS, confirming the permanent deactivation of the catalyst by the formation of a non-active nickel sulfide phase. XRD analysis was carried out on the same specimen used for XAS measurements, and therefore the presence of cellulose is due to the XAS sample preparation procedure. Three reflections at $2\theta \approx 41°$, 37.9° and 36.8° belong to the sample stage. Cellulose peak labelling was carried out according to Park *et al.*[60]

4.3.2 Chlorine poisoning. XRD analysis of the chlorine poisoned catalyst after reaction showed reflections belonging exclusively to zirconia and nickel (*cf.* Fig. 8(b)). The absence of chlorine species was further confirmed by EDX measurements carried out by SEM. This supports the non-persistent nature of chlorine indicated in the catalytic experiment described in section 4.2.2.

The nickel crystallite size was estimated from XRD patterns by applying the Scherrer equation on the $2\theta \approx 44.5°$ reflection. The nickel particle was estimated to be approximately 39 nm for the chlorine exposed sample, indicating a growth of nickel particles during exposure to chlorine. The growth of nickel nanoparticles could be explained by the formation of mobile Ni–Cl species upon reaction of HCl with surface oxides.[61]

In order to investigate in more detail the extent of chlorine poisoning, the deactivation experiment was repeated with a new batch of catalyst and without restoring the chlorine-free feed. XRD and SEM-EDX analyses of the sample after 48 h of TOS did not reveal the presence of chlorine species. Thus, it appears that chlorine species readily will leave nickel when exposed to air and/or hydrogen (during cooling down of the experiment).

4.3.3 Potassium poisoning. Impregnation of KCl on the catalyst resulted in the deposition of KCl crystals on the catalyst surface, as visualized by both STEM-EDX (Fig. 9) and XRD (Fig. 8(c)) measurements on the spent sample. The XRD measurements indicate an average crystallite size of >100 nm, approximately the size limit after which the

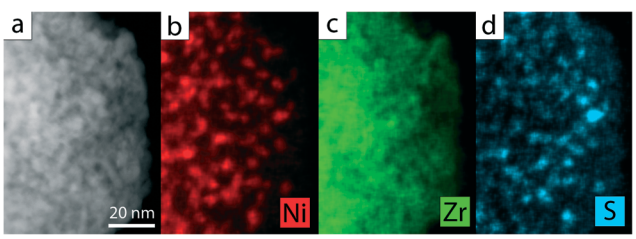

Fig. 7 (a) STEM-HAADF micrograph of the sulfur poisoned catalyst with (b) nickel, (c) zirconium and (d) sulfur EDX elemental distributions.

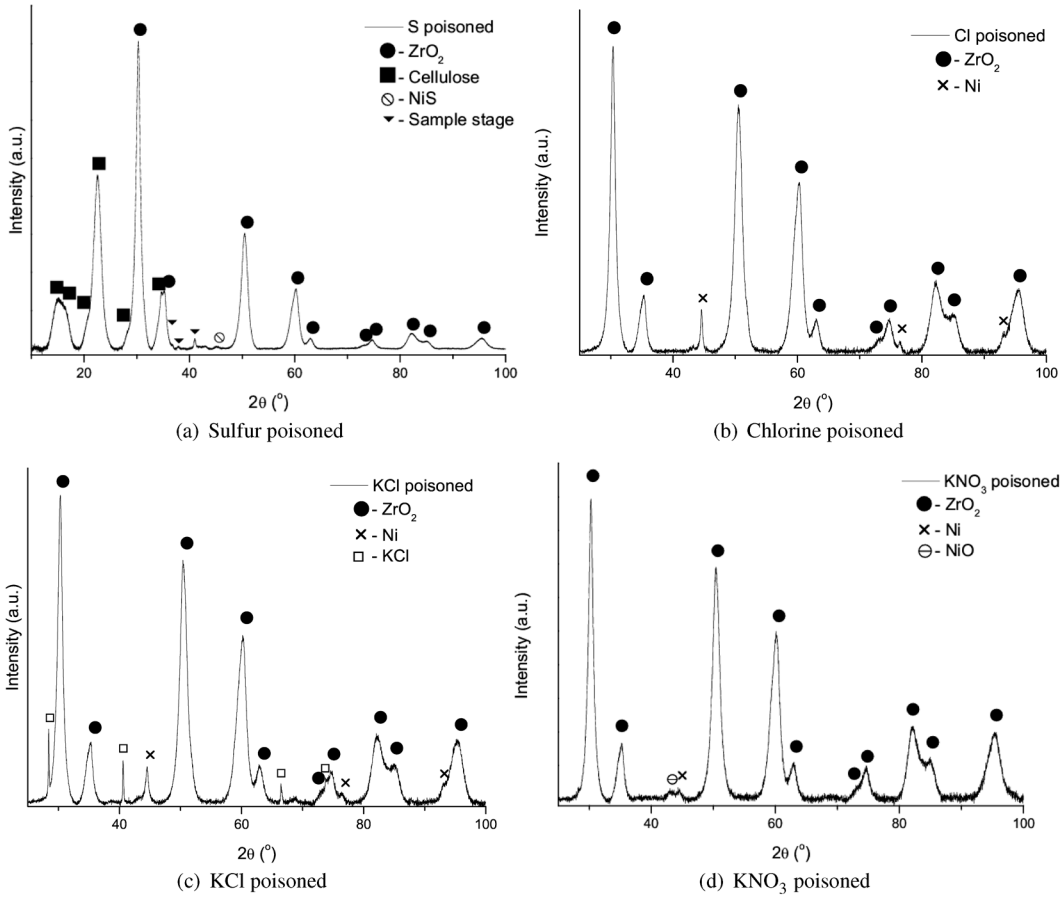

Fig. 8 X-ray diffraction patterns of the poisoned catalysts. (a) Sulfur poisoned catalyst, (b) chlorine poisoned catalyst, (c) KCl poisoned catalyst, (d) KNO_3 poisoned catalyst.

reflection peak width is dominated by instrumental broadening. KCl particle sizes of up to 600 nm were reported as shown by STEM-EDX maps in Fig. 9.

The nickel crystallite size was estimated to be approximately 24 nm for the KCl impregnated catalyst after 25 h TOS, indicating growth of the nickel particle size. However, this was less pronounced when compared to the chlorine poisoned samples but could be explained once more by the presence of HCl during reaction.

Analyzing the spent KNO_3 impregnated catalyst by SEM-EDX confirmed the presence of potassium. However, XRD analysis did not reveal any potassium-containing crystalline phase (*cf.* Fig. 8(d)). This indicates a more homogeneous deposition of potassium compared to that in the KCl impregnated catalyst.

In an attempt to visualize the potassium deposition, STEM-EDX mapping of this catalyst resulted in the redistribution of potassium all over the scanned area. This is due to the high mobility of potassium ions under the effect of the electron beam.[62,63]

4.4 XAS analysis of poisoned catalysts

To further understand the deactivation mechanism of the Ni/ZrO_2 catalyst caused by the impurities in the feed, the local structure of the poisoned samples was analyzed by XAS.

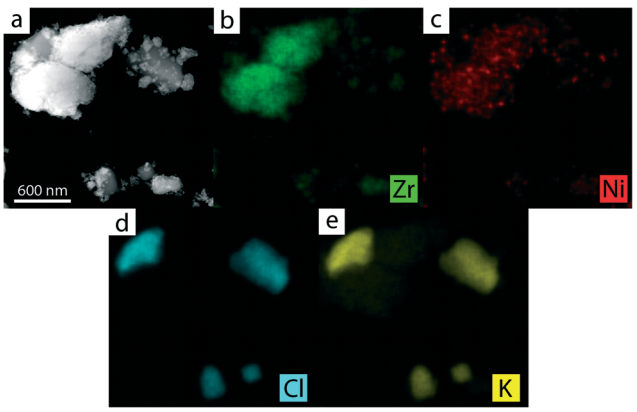

Fig. 9 (a) STEM-HAADF micrograph of the potassium chloride poisoned catalyst with (b) zirconium, (c) nickel, (d) chlorine and (e) potassium EDX elemental distributions.

Table 2 presents the respective refined structural parameters of the investigated samples. Additional information can be found in the ESI.†

Initially, the local structure of the unreduced Ni/ZrO_2-CR and the *in situ* reduction of this catalyst (as discussed in the ESI†) was studied by refining the extended X-ray absorption fine structure (EXAFS) spectra. Table 2 presents the respective

Table 2 Structural parameters around the Ni absorber atom refined from the EXAFS spectra of the Ni/ZrO_2 catalysts, comparing calcined, freshly reduced, and poisoned samples. Calcined is the fresh catalyst prior to reduction and reduced is the same catalyst after *in situ* reduction. *N* is the number of neighboring atoms, *r* the distance, σ^2 the mean-square disorder in the atomic distances, and ρ the misfit between experimental data and theory. $S_0^2 = 0.78$, calcined: $\Delta E_0 = -3.5 \pm 0.5$, reduced: $\Delta E_0 = 6.5 \pm 0.6$, carbon: $\Delta E_0 = 5.8 \pm 0.9$, chlorine: $\Delta E_0 = 6.6 \pm 1.4$, KCl: $\Delta E_0 = 7.1 \pm 0.7$, KNO_3: $\Delta E_0 = 6.6 \pm 1.0$ and $C_3 = 4.9 \times 10^{-4}$ Å^3, sulfur: $\Delta E_0 = 8.4 \pm 0.5$

Sample	Shell	Atom	*N*	*r* [Å]	$\sigma^2 \times 10^{-3}$ [Å^2]	ρ [%]
Calcined	1st	O	6.0[c]	2.06[a,e]	6.2 ± 0.5[e]	0.7
	2nd	Ni	8.6 ± 0.9[e]	2.96[a,e]	9.6 ± 1.0[e]	
Reduced	1st	Ni	9.2 ± 1.0[e]	2.48 ± 0.01[e]	5.5 ± 0.8[e]	3.2
	2nd	Ni	6.9 ± 3.4[e]	3.46 ± 0.02[e]	14.0 ± 0.5[e]	
	3rd	Ni	21.6 ± 7.8[e]	4.33± 0.01[e]	10.2± 3.3[e]	
Carbon poisoned[b]	1st	O	0.8 ± 0.3[e]	1.98 ± 0.05[e]	7.1 ± 0.1[d,e]	0.5
	2nd	Ni	8.7 ± 0.9[e]	2.48 ± 0.01[e]	6.3 ± 1.0[e]	
Chlorine poisoned	1st	O	0.8 ± 0.2[e]	2.00± 0.04[e]	7.2 ± 0.1[a,e]	0.9
	2nd	Ni	8.5 ± 0.6[e]	2.48[a,e]		
KCl poisoned	1st	O	0.6 ± 0.1[e]	2.00 ± 0.04[e]	7.2 ± 0.1[a,e]	0.9
	2nd	Ni	9.9 ± 0.4[e]	2.48[a,e]	6.8 ± 0.5[e]	
KNO_3 poisoned	1st	O	1.1 ± 0.3[e]	1.96 ± 0.01[e]	7.9 ± 4.5[a,e]	1.3
	2nd	Ni	8.3 ± 0.9[e]	2.48 ± 0.01[e]	9.2 ± 1.0[e]	
Sulfur poisoned	1st	S	5.0[c]	2.22 ± 0.01[e]	7.6 ± 0.4[e]	2.5

[a] Fitted uncertainty less than 1%. [b] Ni/ZrO_2-DR used in the long term testing in section 1 analyzed after 106 h TOS. [c] Constrained. [d] Ni–O σ^2 was constrained and fitted together with a $NiCO_3$ reference. [e] Fitted.

refined structural parameters. For the calcined catalyst, nickel was coordinated by 6 oxygen atoms at 2.06 Å, and the second coordination shell was composed of 8.6 ± 0.9 nickel atoms at 2.96 Å. This local order was similar to NiO as expected; however, the number of nickel atoms at the second coordination shell was lower than that for NiO (12 nickel atoms[64]), which indicates a small particle size of the NiO-like structure after calcination.

The local chemical environment of the reduced catalyst was similar to a metallic nickel phase; nevertheless, the refined 9.2 ± 1.0 coordination number of the first shell showed that the reduced phase of the catalyst was structured as small particles.

Analyzing the poisoned catalyst samples, the local nickel surroundings in the KNO_3, KCl, chlorine, and carbon (catalyst exposed to feed for 106 h TOS) poisoned catalysts remained similar to the reduced catalyst as seen from the refined structural parameters in Table 2 with the exception of a slight oxidation after reaction. This was evidenced by a peak shoulder around 2 Å at the Fourier transformed EXAFS spectra (see the ESI†). These oxygen atoms were most likely at the surface of the nickel metallic particles since the refined bond distances, varying between 1.96–2.00 Å, were shorter than the expected Ni–O distance in the NiO reference (2.08 Å).[64] The oxidation was probably a consequence of exposure to air in between the experiment and XAS measurements, as confirmed in the XRD pattern of potassium and chlorine poisoned catalysts (*cf.* Fig. 8) by the presence of a weak peak at $2\theta \approx 43°$, corresponding to a NiO phase.

The Fourier transformed EXAFS spectra of the carbon and KCl poisoned catalysts presented a significant amplitude reduction (see the ESI†). The structural refinements showed that this amplitude reduction was mainly caused by the increase of the structural disorder expressed by the mean-square disorder in the atomic distances.

The KNO_3 poisoned catalyst showed the strongest amplitude reduction as a result of high structural disorder. The refinement of its EXAFS spectrum required an additional structural parameter (the third cumulant of disorder, C_3), which measures the asymmetry of atomic vibrations. A reduction in the magnitude of the Ni signal was also observed in the XRD pattern of this catalyst (*cf.* Fig. 8). Note that in both the Fourier transformed EXAFS spectra (see the ESI†) and the EXAFS fit (*cf.* Table 2) there was a stronger contribution for backscattering at low *R* values. This provides evidence of stronger oxidation.

Overall, these XAS measurements support the observations in section 4.3 that chlorine and alkali metals did not induce a phase change of nickel crystals. Thus, the deactivation caused by these species was probably related to deposition on the nickel surface.

The Ni-K-edge XANES of the sulfur poisoned catalyst sample showed the presence of a completely different Ni species, as shown in Fig. 10. The refinements suggested the conversion of the metallic Ni phase to a NiS-like phase, which explains the total loss of the catalytic activity in this case. This is supported by the STEM-EDX map in Fig. 7, also showing that sulfur is distributed similar to Ni, confirming the tight interaction and the reflection of NiS in the XRD pattern (*cf.* Fig. 8(a)).

4.5 Comparison of deactivation mechanisms

For a quantitative comparison of the different deactivation phenomena, the kinetic constants (*cf.* section 3) for the four reactions were calculated, as summarized in Table 3. Sulfur was the worst poison as this catalyst was completely inactive with respect to both hydrogenation and deoxygenation after a relatively short exposure time.

XRD, STEM-EDX, and EXAFS analyses revealed that the sulfur deactivated catalyst was a bulk deactivation (*cf.* Fig. 10),

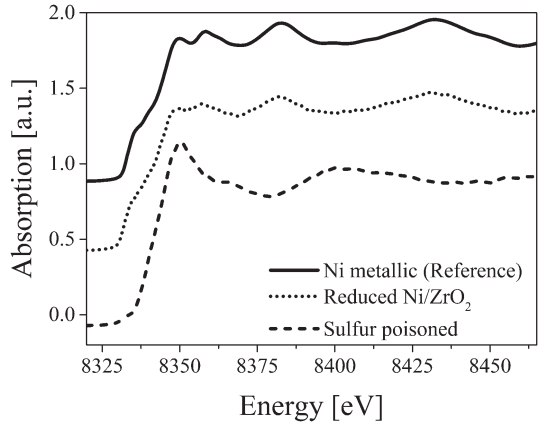

Fig. 10 Ni-K edge X-ray absorption spectra of the sulfur poisoned catalyst compared to fresh Ni/ZrO_2 and Ni reference.

Table 3 Rate constants for the HDO of guaiacol and 1-octanol deactivated with different poisons relative to the case shown in Fig. 5(b) with Ni/ZrO_2-DR and no poison. The effectiveness factor was in the order of 89–97% for the fastest reactions. TOS refers to when the kinetic parameters are evaluated in comparison to Fig. 5 and 6. T = 250 °C, P = 100 bar, F_{oil} = 0.2 ml min^{-1}, WHSV = 4.0 h^{-1}

	TOS	Exposure	k_1'	k_2'	k_3'	k_4'
Poison	[h]	[mol_{poison} mol_{Ni}^{-1}]	[ml kg_{cat}^{-1} min^{-1}]			
None[a]	—	—	607	124	80	602
Carbon[b]	104	3×10^4	>500	108	52	>500
Sulfur	23	1.1	0	0	0	0
Chlorine	48	3.2	181	25	6.1	20
KCl	11	1	>500	26	0.6	22
KNO_3	12	1	>500	53	0	24

[a] Determined from an intrinsic activity measurement with 1.5 g of 5 wt% Ni/ZrO_2 in a sieve fraction of 125–180 μm but otherwise similar experimental conditions with an effectiveness factor of ≥99% for the fastest reactions. [b] Ni/ZrO_2-DR used in long term testing in section 4.1.

which explains the distinct deactivation profile (*cf.* Fig. 6(a)). It has previously been shown that sulfur forms a saturated surface layer on nickel at p_{H_2S}/p_{H_2} ratios above 5×10^{-6}.[65] The p_{H_2S}/p_{H_2} threshold for the formation of bulk sulfides decreases with decreasing temperatures and is in the order of 10^{-4} at 400 °C[66] but even lower at 250 °C. In the current experiment the p_{H_2S}/p_{H_2} ratio was 2×10^{-4}, assuming all 1-octanethiol decomposed to H_2S, which is at the range where bulk nickel sulfides can be expected to form.

Sulfur deactivation of nickel catalysts has previously been established to be severely persistent and hardly reversible in hydrogen alone.[67,68] Removal of sulfur can be achieved to some extent by steaming of the catalyst, but this requires temperatures above 600–650 °C.[69,70] Thus, the catalyst appears to have little chance to avoid deactivation or to regain activity in the presence of sulfur species during HDO. Our results therefore do not confirm the observations by Song *et al.*[26,27] that a high hydrogen pressure can retain Ni in an active state in HDO. The reason for this difference is not clear but may be related to the fact that Song *et al.* made experiments in a batch reactor where deactivation phenomena are generally difficult to observe, especially if the reactor is overloaded with catalyst.

In steam reforming, where nickel catalysts have been extensively used, alkali metals are known to readily deactivate the catalyst.[28,29,55,71] Bengaard *et al.*[54] showed that the deactivation of nickel catalysts for steam reforming by alkali metals was due to adsorption at the step sites on the nickel crystallites.

In this study, doping with potassium hindered the deoxygenation reactions (k_2', k_3', and k_4' in Table 3), while the hydrogenation reaction was less affected. This correlates with the Ni/ZrO_2 catalyst having two different types of active sites: vacancy sites in the oxide support where phenolic compounds can adsorb prior to hydrogenation and exposed low coordinated metal sites facilitating the deoxygenation reactions.[51] Thus, it appears that potassium (and maybe also chlorine) preferentially interacts with low coordinated nickel sites, as primarily the deoxygenation reactions were affected.

The most striking difference in the deactivation by chlorine and potassium was the reversibility of chlorine poisoning. This reversibility of chlorine adsorption has also been observed previously.[72–75] During methane steam reforming over Ni/Al_2O_3, Ortego *et al.*[74] observed that the reforming activity decreased when co-feeding CH_3Cl. However, the activity was regained when removing the chlorine source from the feed. Richardson *et al.*[73] also found that the presence of chlorocarbons in the feed led to a decrease in the methane steam reforming activity of the Ni/Al_2O_3 catalyst. They concluded that chlorine formed an equilibrium surface layer on the nickel, which at high coverage could deplete the availability of hydrogen. Similarly, Kiskinova and Goodman[72] found that the poisoning effect on CO and H_2 adsorption on a Ni (100) surface increased in the order of P < S < Cl. However, despite Cl being the worst poison, it easily reacted with H_2 to form HCl. Thus, if the chlorine surface layer was not maintained, chlorine was found to not affect the catalytic activity for methanation.

In summary, the current and previous studies show that chlorine primarily affects the catalytic activity when fed to the reactor as the coverage appears to be determined by a fast adapting equilibrium with hydrogen and HCl. This is supported by the identification of Cl^- in the liquid product after ending the exposure to chlorooctane. However, investigation on the particle size by XRD did indicate that chlorine also causes the sintering of nickel particles on the catalyst.

Impregnation with KCl and KNO_3 shows similar trends. Deactivation by KCl, however, was slightly worse, especially considering the hydrogenolysis reaction (k_2). This may be linked to the sintering induced by the presence of chlorine.

5. Conclusion

In this study, the stability and resistance of Ni/ZrO_2 have been investigated during long term operation in a continuous

flow setup for the HDO of a mixture of 10% guaiacol in 1-octanol as a model system for bio-oil.

The stability and activity of the catalyst were dependent on the nickel particle size. Small nickel particles (9 nm) gave higher activity for HDO and produced less coke on the catalyst compared to larger particles (18 nm). Over a period of more than 100 h of operation a carbon build-up of only 1.5 wt% relative to the catalyst mass occurred for the 9 nm Ni/ZrO_2 catalyst and therefore the activity only decreased slightly from a DOD of 92% on the fresh catalyst to a DOD of 90% after 104 h TOS. The higher activity of the small crystallites was linked to their higher fraction of low coordinated sites which are efficient in the deoxygenation reaction. The smaller particle size was also responsible for lower carbon deposition since it is more difficult for carbon to form on these.

The catalyst stability was very sensitive to sulfur, chlorine, and potassium exposure. Addition of sulfur to the feed resulted in a fast deactivation of the catalyst, leading to the complete loss of activity over a period of only 12 h, which was roughly the time required to feed the stoichiometric amount of sulfur relative to the available nickel. In line with this, STEM-EDX, XRD, and XAS measurements unraveled the formation of a NiS-like phase, which was the reason for the complete loss of activity for this catalyst.

Chlorine did not deactivate the catalyst to the same extent as sulfur, as primarily the deoxygenation activity decreased after exposure to chlorine over a 40 h period, corresponding to the addition of 3.2 mol Cl : 1 mol Ni. Furthermore, the deactivation by chlorine was reversible as the activity could be partly regained when removing chlorine from the feed. XRD, XAS, or EDX could not identify chlorine on the spent catalyst, supporting the reversibility of the deactivation mechanism. It is suggested that chlorine binds to the nickel surface sites (preferentially low coordinated sites) and forms an equilibrium surface layer, but when not co-feeding Cl this layer is easily removed. However, chlorine also appeared to cause sintering of nickel particles on the catalyst, providing a more persistent deactivation/activity loss.

KCl and KNO_3 were impregnated on two different batches of catalyst to test the effect of potassium. The hydrogenation activity was not affected in any significant degree in the two cases, but the deoxygenation activity was markedly decreased and was persistent over more than 20 h of operation. Probably, potassium blocked low coordinated sites leading to the loss of deoxygenation activity, as these are considered crucial for this reaction.

Comparing the different poisons, sulfur was the most severe, while potassium and chlorine were in the same order of magnitude when looking at the activity. However, as potassium is a persistent poison this must be considered more severe than chlorine.

An overall conclusion is that it is difficult to obtain long term stability for nickel based catalysts for bio-oil HDO as any of the three types of poisons tested will lead to deactivation. From an application point of view it would be crucial to remove specifically sulfur from the feed beforehand and to minimize potassium and chlorine impurities. The present work shows the importance of studying the stability of catalysts for HDO of bio-oil under more realistic conditions.

Acknowledgements

This work is part of the Combustion and Harmful Emission Control (CHEC) research center at The Department of Chemical and Biochemical Engineering at the Technical University of Denmark (DTU). The present work is financed by DTU and The Catalysis for Sustainable Energy initiative (CASE), funded by the Danish Ministry of Science, Technology and Innovation.

The A. P. Møller and Chastine Mc-Kinney Møller Foundation is gratefully acknowledged for its contribution towards the establishment of the Center for Electron Nanoscopy at the Technical University of Denmark.

The Interdisciplinary Centre for Electron Microscopy (CIME) at EPFL is gratefully acknowledged for the use of the FEI Tecnai Osiris TEM.

We thank ANKA for providing beamtime and Stefan Mangold, Henning Lichtenberg, and Alexey Boubnov for help during or around beamtime.

BMBF is acknowledged for the support of the *in situ* infrastructure at ANKA (KIT, Karlsruhe) within the MatAkt project (05K10VKB).

References

1 P. M. Mortensen, J.-D. Grunwaldt, P. A. Jensen, K. G. Knudsen and A. D. Jensen, *Appl. Catal., A*, 2011, **407**, 1–19.
2 A. V. Bridgwater, S. Czernik, J. Diebold, D. Meier, A. Oasmaa, C. Peakocke, J. Piskorz and D. Radlein, *Fast Pyrolysis of Biomass: A Handbook*, CPL Press, Newbury, 1999.
3 J. Holmgren, R. Marinageli, P. Nair, D. C. Elliott and R. Bain, *Hydrocarbon Process.*, 2008, 95–103.
4 K. Raffelt, E. Henrich, A. Koegel, R. Stahl, J. Steinhardt and F. Weirich, *Appl. Biochem. Biotechnol.*, 2006, **129**, 153–164.
5 Q. Zhang, J. Chang, T. Wang and Y. Xu, *Energy Convers. Manage.*, 2007, **48**, 87–92.
6 T. V. Choudhary and C. B. Phillips, *Appl. Catal., A*, 2011, **397**, 1–12.
7 Q. Bu, H. Lei, A. H. Zacher, L. Wang, S. Ren, J. Liang, Y. Wei, Y. Liu, J. Tang, Q. Zhang and R. Ruan, *Bioresour. Technol.*, 2012, **124**, 470–477.
8 Z. He and X. Wang, *Catal. Sustainable Energy Prod.*, 2012, **1**, 28–52.
9 E. Furimsky, *Catal. Today*, 2013, **217**, 13–56.
10 H. Wang, J. Male and Y. Wang, *ACS Catal.*, 2013, **3**, 1047–1070.
11 D. C. Elliott, *Energy Fuels*, 2007, **21**, 1792–1815.
12 I. Graca, J. M. Lopes, H. S. Cerqueira and M. F. Ribeiro, *Ind. Eng. Chem. Res.*, 2012, **52**, 275–287.
13 D. C. Elliott, T. R. Hart, G. G. Neuenschwander, L. J. Rotness and A. H. Zacher, *Environ. Prog. Sustainable Energy*, 2009, **28**, 441–449.
14 D. C. Elliott and T. R. Hart, *Energy Fuels*, 2009, **23**, 631–637.

15 J. Wildschut, F. H. Mahfud, R. H. Venderbosch and H. J. Heeres, *Ind. Eng. Chem. Res.*, 2009, **48**, 10324–10334.
16 J. Wildschut, J. Arentz, C. B. Rasrendra, R. H. Venderbosch and H. J. Heeres, *Environ. Prog. Sustainable Energy*, 2009, **28**, 450–460.
17 V. A. Yakovlev, S. A. Khromova, O. V. Sherstyuk, V. O. Dundich, D. Y. Ermakov, V. M. Novopashina, M. Y. Lebedev, O. Bulavchenko and V. N. Parmon, *Catal. Today*, 2009, **144**, 362–366.
18 M. V. Bykova, D. Y. Ermakov, V. V. Kaichev, O. Bulavchenko, A. A. Saraev, M. Y. Lebedev and V. A. Yakovlev, *Appl. Catal., B*, 2012, **113–114**, 296–307.
19 M. V. Bykova, S. G. Zavarukhin, L. I. Trusov and V. A. Yakovlev, *Kinet. Catal.*, 2013, **54**, 40–48.
20 V. O. Dundich, S. A. Khromova, D. Y. Ermakov, M. Y. Lebedev, V. M. Novopashina, V. G. Sister, A. I. Yakimchuk and V. A. Yakovlev, *Kinet. Catal.*, 2010, **51**, 728–734.
21 P. M. Mortensen, J.-D. Grunwaldt, P. A. Jensen and A. D. Jensen, *ACS Catal.*, 2013, **3**, 1774–1785.
22 A. V. Bridgwater, *Catal. Today*, 1996, **29**, 285–295.
23 E. Furimsky and F. E. Massoth, *Catal. Today*, 1999, **52**, 381–495.
24 G. W. Huber, S. Iborra and A. Corma, *Chem. Rev.*, 2006, **106**, 4044–4098.
25 T. N. Trinh, P. A. Jensen, H. R. Sørensen, K. Dam-Johansen and S. Hvilsted, *Energy Fuels*, 2013, **27**, 1399–1409.
26 Q. Song, C. Wang and J. Xu, *Chem. Commun.*, 2012, **48**, 7019–7021.
27 Q. Song, F. Wang, J. Cai, Y. Wang, J. Zhang, W. Yu and J. Xu, *Energy Environ. Sci.*, 2013, **6**, 994–1007.
28 K. Aasberg-Petersen, T. S. Christensen, I. Dybkjær, J. Sehested, M. Østberg, R. M. Coertzen, M. J. Keyser and A. P. Steynberg, in *Fischer-Tropsch Technology*, Elsevier, Amsterdam, 2004, ch. 4: Synthesis Gas Production for FT Synthesis, pp. 258–405.
29 J. R. Rostrup-Nielsen, in *Handbook of Heterogeneous Catalysis*, John Wiley & Sons, Inc., New York, 2008, ch. 13.11: Steam Reforming, pp. 2882–2905.
30 P. R. Patwardhan, R. C. Brown and B. H. Shanks, *ChemSusChem*, 2011, **4**, 1629–1636.
31 M. S. A. Moraes, M. V. Migliorini, F. C. Damasceno, F. Georges, S. Almeida, C. A. Zini, R. A. Jacques and E. B. Caramão, *J. Anal. Appl. Pyrolysis*, 2012, **98**, 51–64.
32 E. Furimsky, *Appl. Catal., A*, 2000, **199**, 144–190.
33 E. Laurent, A. Centeno and B. Delmon, *Stud. Surf. Sci. Catal.*, 1994, **88**, 573–578.
34 H. S. Fogler, *Elements of Chemical Reaction Engineering*, Prentice Hall, New Jersey, 2006.
35 *CRC Handbook of Chemistry and Physics 92th Edition (Internet Version 2012)*, ed. W. M. Haynes, CRC Press, April 2010.
36 K. Schofield, *Prog. Energy Combust. Sci.*, 2008, **34**, 330–350.
37 P. L. Llewellyn, E. Bloch and S. Bourelly, in Surface Area/Porosity, Adsorption, Diffusion, *Characterization of Solid Material and Heterogenous Catalysts*, Wiley-VCH, Weinheim, 2012, ch. 19: Surface Area/Porosity, Adsorption, Diffusion, pp. 853–880.
38 J.-D. Grunwaldt, S. Hannemann, J. Göttlicher, S. Mangold, M. Denecke and A. Baiker, *Phys. Scr., T*, 2005, **115**, 769–772.
39 J.-D. Grunwaldt, M. Caravati, S. Hannemann and A. Baiker, *Phys. Chem. Chem. Phys.*, 2004, **6**, 3037–3047.
40 J.-D. Grunwaldt, N. van Vegten and A. Baiker, *Chem. Commun.*, 2007, 4635–4637.
41 B. Ravel and M. Newville, *J. Synchrotron Radiat.*, 2005, **12**, 537–541.
42 J. J. Rehr, J. J. Kas, M. P. Prange, A. P. Sorini, Y. Takimoto and F. D. Vila, *C. R. Phys.*, 2009, **10**, 548–559.
43 C. Zhao, J. He, A. A. Lemonidou, X. Li and J. A. Lercher, *J. Catal.*, 2011, **280**, 8–16.
44 Y.-C. Lin, C.-L. Li, H.-P. Wan, H. Lee and C.-F. Liu, *Energy Fuels*, 2011, **25**, 890–896.
45 C. R. Lee, J. S. Yoon, Y.-W. Suh, J.-W. Choi, J.-M. Ha, D. J. Suh and Y.-K. Park, *Catal. Commun.*, 2012, **17**, 54–58.
46 B. Peng, C. Zhao, I. Mejía-Centeno, G. A. Fuentes, A. Jentys and J. A. Lercher, *Catal. Today*, 2012, **183**, 3–9.
47 J. Ryu, S. M. Kim, J.-W. Choi, J.-M. Ha, D. J. Ahn, D. J. Suh and Y.-W. Suh, *Catal. Commun.*, 2012, **29**, 40–47.
48 I. Barin, *Thermochemical Data of Pure Substances*, VCH, Weinheim, 1989.
49 S. J. Hurff and M. T. Klein, *Ind. Eng. Chem. Fundam.*, 1983, **22**, 426–430.
50 C. Louis, Z. X. Cheng and M. Che, *J. Phys. Chem.*, 1993, **97**, 5703–5712.
51 P. M. Mortensen, *Ph.D. thesis*, Technical University of Denmark, 2013.
52 S. W. Benson, *Thermochemical Kinetics: Methods for estimation of thermochemical data and rate parameters*, John Wiley & Sons, Inc., New York, 1968.
53 T. Borowiecki, *Appl. Catal.*, 1982, **4**, 223–231.
54 H. S. Bengaard, J. K. Nørskov, J. Sehested, B. S. Clausen, L. P. Nielsen, A. M. Molenbroek and J. R. Rostrup-Nielsen, *J. Catal.*, 2002, **209**, 365–384.
55 J. R. Rostrup-Nielsen, J. Sehested and J. K. Nørskov, *Adv. Catal.*, 2002, **47**, 65–139.
56 G. Tavoularis and M. A. Kean, *J. Mol. Catal. A: Chem.*, 1999, **142**, 187–199.
57 C. Menini, C. Park, E.-J. Shin, G. Tavoularis and M. A. Keane, *Catal. Today*, 2000, **62**, 355–366.
58 B. Schrick, J. L. Blough, A. D. Jones and T. E. Mallouk, *Chem. Mater.*, 2002, **14**, 5140–5147.
59 M. A. Keane, *ChemCatChem*, 2011, **3**, 800–821.
60 S. Park, J. O. Baker, M. E. Himmel, P. A. Parilla and D. K. Johnson, *Biotechnol. Biofuels*, 2010, **3**.
61 Y. Ohtsuka, *J. Mol. Catal.*, 1989, **54**, 225–235.
62 K. Jurek and O. Gedeon, *Microchim. Acta*, 2008, **161**, 377–380.
63 S. Hodson and J. Marshall, *J. Microsc.*, 1971, **93**, 49–53.
64 S. Sasaki, K. Fujino and Y. Takeuchi, *Proc. Jpn. Acad., Ser. B*, 1979, **55**, 43–48.
65 J. R. Rostrup-Nielsen, *J. Catal.*, 1968, **11**, 220–227.
66 T. Rosenqvist, *J. Iron Steel Inst., London*, 1954, **176**, 37–57.
67 J. L. Oliphant, R. W. Fowler, R. B. Pannell and C. H. Bartholomew, *J. Catal.*, 1978, **51**, 229–242.
68 C. H. Bartholomew, G. D. Weatherbee and G. A. Jarvi, *J. Catal.*, 1979, **60**, 257–269.

69 J. R. Rostrup-Nielsen, *J. Catal.*, 1971, **21**, 171–178.
70 H. Oudghiri-Hassani, N. Abatzoglou, S. Rakass and P. Rowntree, *J. Power Sources*, 2007, **171**, 811–817.
71 T. S. Christensen, *Appl. Catal., A*, 1996, **138**, 285–309.
72 M. Kiskinova and D. W. Goodman, *Surf. Sci.*, 1981, **108**, 64–76.
73 J. T. Richardson, J. D. Ortego, N. Coute and M. V. Twigg, *Catal. Lett.*, 1996, **41**, 17–20.
74 J. D. Ortego, J. T. Richardson and M. V. Twigg, *Appl. Catal., B*, 1997, **12**, 339–355.
75 J. P. Trembly, R. S. Gemmen and D. J. Bayless, *J. Power Sources*, 2007, **169**, 347–354.

